Supplementary Information for

Freeform terahertz structures fabricated by multi-photon lithography and metal coating

Pascal Maier,[1,2] Alexander Kotz,[1] Joachim Hebeler,[3] Qiaoshuang Zhang,[4] Christian Benz,[1,2] Alexander Quint,[3] Marius Kretschmann,[3] Tobias Harter,[1] Sebastian Randel,[1] Uli Lemmer,[4] Wolfgang Freude,[1] Thomas Zwick,[3] and Christian Koos[1,2,5,*]

[1]*Institute of Photonics and Quantum Electronics (IPQ), Karlsruhe Institute of Technology (KIT), Engesserstrasse 5, 76131 Karlsruhe, Germany*
[2]*Institute of Microstructure Technology (IMT), KIT, Hermann-von-Helmholtz-Platz 1, 76344 Eggenstein-Leopoldshafen, Germany*
[3]*Institute of Radio Frequency Engineering and Electronics (IHE), KIT, Engesserstrasse 5, 76131 Karlsruhe, Germany*
[4]*Light Technology Institute (LTI), KIT, Engesserstrasse 13, 76131 Karlsruhe, Germany*
[5]*Teragear GmbH, Seboldstrasse 22, 76227 Karlsruhe, Germany*
* christian.koos@kit.edu

This document provides supplementary information to “Freeform terahertz structures fabricated by multi-photon lithography and metal coating”. In Section 1, we report on the measurements of the dielectric response of the photoresist used for multi-photon lithography (MPL). Section 2 gives more insights into the design of the THz structures. The results of the surface roughness measurements of the metal-coated freeform structures (MCFS) and coplanar-waveguide (CPW) feeds are given in Section 3. Section 4 investigates the influence of the metal conductivity on the device performance. Details on the measurement setups and procedures for the THz interconnects (TIC), the THz probes (TP) and the THz antennas (TA) can be found in Sections 5, 6, and 7, respectively. Section 8 finally summarizes mathematical relations for converting between *S*-parameters and *T*-matrix parameters.

1. Dielectric response of the photoresist

For precise simulation and design of the THz structures, the frequency-dependent dielectric response of the photoresist used for the 3D-printed support structures (VanCore B, Vanguard Automation GmbH, Karlsruhe, Germany) must be known. We therefore measured the complex-valued relative permittivity $\underline{\varepsilon}_\mathrm{r} = \varepsilon' - \mathrm{j}\varepsilon''$ of a photoresist sample in the frequency range between 0.220 THz and 0.325 THz using a commercially available material-characterization kit (MCK, Swissto12 SA, Renens, Switzerland).

The measurement setup is shown in Fig. S1a. A pair of WR-3 frequency-extension modules (V03VNA2-T/R-A, OML Inc., Morgan Hill, USA) are connected to a vector network analyzer (VNA, N5242B PNA-X, Keysight Technologies Inc., Santa Rosa, USA) via a millimeter-wave controller (N5292A, Keysight Technologies Inc.). In conjunction with the frequency-extension modules, the VNA enables *S*-parameter measurements in a frequency range from 0.220 THz to 0.325 THz. The VNA is set to measure at 1001 frequency points with an intermediate-frequency (IF) bandwidth of 500 Hz. The MCK is directly connected to the frequency-extension modules via UG-387/UM waveguide flanges. The MCK itself consists of two corrugated horn antennas[1], effectively converting the input TE10 mode of the rectangular waveguides to a highly pure HE_{11} mode of the circular horn-antenna aperture. This allows for a plane-wave-like irradiation of the dielectric sample, which is placed in the gap between the two antennas. Prior to the actual measurement, the setup is calibrated using the gated-reflect-line (GRL) calibration technique[2]. Time-domain gating with a manufacturer-recommended window size of 400 ps is employed to isolate the characteristics of the MCK setup. The “Through” standard is then realized by closing the gap between the pair of corrugated antennas without any sample inserted, thereby normalizing $\underline{S}_{21}$. Finally, the “Reflect” standard is realized by inserting a 1 mm-thick metal shim into the gap, effectively acting as a perfect metal reflector for normalizing $\underline{S}_{11}$.

As a sample, we use a 380 µm-thick plate of photoresist which was fabricated via spin coating, followed by UV curing at a wavelength of 365 nm and subsequent heat curing at 85°C for one hour. The maximum thickness variation across the plate with roughly 11 mm diameter was measured to be of the order of ± 10 µm. A picture of the photoresist sample is shown in the zoom-in in Fig. S1a. After clamping the sample between the two corrugated horn antennas, *S*-parameter measurements are taken. With the knowledge of the sample thickness, the real and imaginary parts of the permittivity, $\Re(\underline{\varepsilon}_\mathrm{r}) = \varepsilon'$ and $-\Im(\underline{\varepsilon}_\mathrm{r}) = \varepsilon''$, can be extracted from the acquired $\underline{S}_{21}$ and $\underline{S}_{11}$ parameters using a manufacturer-provided evaluation software[3]. Note that the results of this approach have been shown to lead to excellent agreement[4] with quasi-standard permittivity-measurement procedures developed by the National Institute of Standards and Technology (NIST)[5,6]. The measured frequency-dependent real and imaginary parts of the permittivity of our sample are shown in Fig. S1b, see left panel for $\Re(\underline{\varepsilon}_\mathrm{r}) = \varepsilon'$ and right panel for $-\Im(\underline{\varepsilon}_\mathrm{r}) = \varepsilon''$. The solid blue lines represent the results obtained when evaluating the measured data for the mean sample thickness of 380 µm, whereas the dashed lines correspond to the respective estimated upper and lower limits as given by the uncertainty of the sample thickness (± 10 µm). From the extracted data, we find an average relative uncertainty of $\Delta\varepsilon'/\varepsilon' \approx 5.1\%$ and $\Delta\varepsilon''/\varepsilon'' \approx 10.8\%$ for the real and imaginary parts, respectively. Figure S1c shows the frequency-

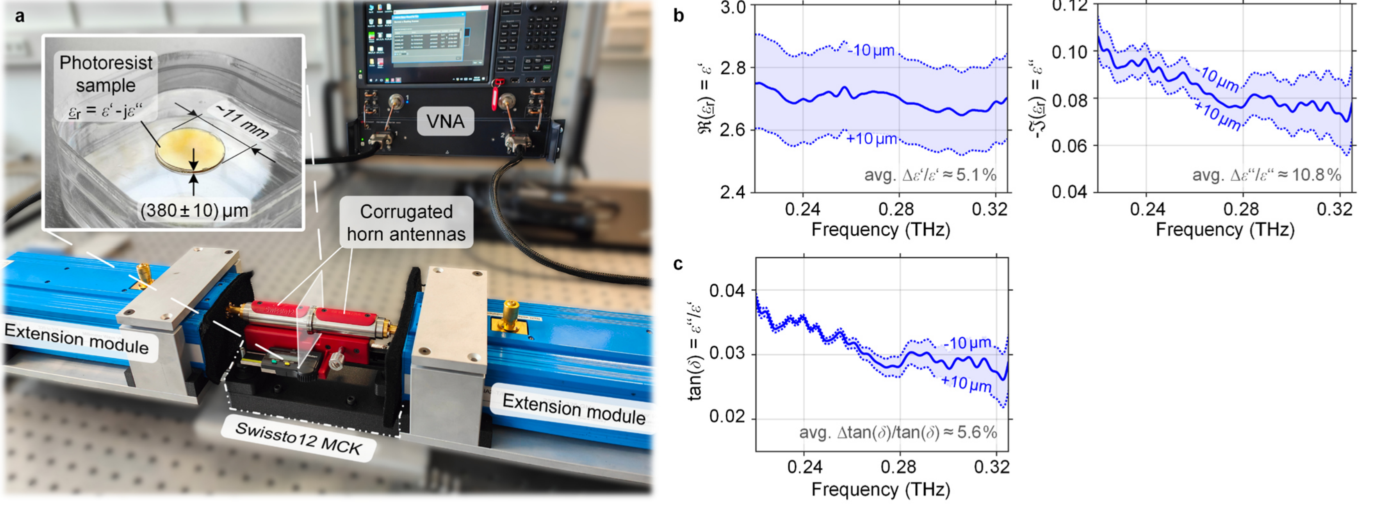

Fig. S1 | Permittivity measurement of multi-photon-lithography resist. **a** Measurement setup, comprising a pair of frequency-extension modules connected to a vector network analyzer (VNA) to enable *S*-parameter measurements in a frequency range from 0.220 THz to 0.325 THz. A commercially available material-characterization kit (MCK, Swissto12) is directly connected to the frequency-extension modules. The MCK consists of two corrugated horn antennas providing a plane-wave-like irradiation of a 380 µm-thick photoresist sample, which is placed in the gap between the two antennas, see zoom-in. **b** Measured frequency-dependent real part $\Re(\underline{\varepsilon}_r) = \varepsilon'$ (left panel) and imaginary part $-\Im(\underline{\varepsilon}_r) = \varepsilon''$ (right panel) of the complex-valued permittivity $\underline{\varepsilon}_r = \varepsilon' - j\varepsilon''$. The solid blue lines represent the results as evaluated using the mean sample thickness of 380 µm, whereas the dashed lines correspond to the respective estimated upper and lower limits as given by the uncertainty of the sample thickness of ±10 µm. From the extracted data, we find an average relative uncertainty of $\Delta\varepsilon'/\varepsilon' \approx 5.1\%$ and $\Delta\varepsilon''/\varepsilon'' \approx 10.8\%$ for the real and imaginary parts, respectively. **c** Measured frequency-dependent loss tangent $\tan(\delta) = \varepsilon''/\varepsilon'$ calculated from the real and imaginary parts of the permittivity as given in Subfigure b. Again, the solid blue line represents the result for the mean sample thickness whereas the dashed lines correspond to the respective estimated upper and lower limits. We find an acceptable average relative uncertainty of $\Delta\tan(\delta)/\tan(\delta) \approx 5.6\%$.

dependent loss tangent $\tan(\delta) = \varepsilon''/\varepsilon'$ calculated from the real and imaginary parts of the permittivity as given in Fig. S1b. Again, the solid blue line represents the result for the mean sample thickness, whereas the dashed lines correspond to the respective estimated upper and lower limit. We find an average relative uncertainty of $\Delta\tan(\delta)/\tan(\delta) \approx 5.6\%$. The measured values for the real part of the permittivity of the order of $\varepsilon' \approx 2.5 - 2.9$ and for the loss tangent of the order of $\tan(\delta) \approx 0.02 - 0.04$ are in good agreement with reported characteristics of other multi-photon printable photoresists, e.g., SU-8, see ref. 7. Note also that the reported uncertainties are in good agreement with previously reported measurement uncertainties using the same MCK measurement system[8]. The material characteristics of the 3D-printed support structures are subsequently modeled using the depicted results of the dielectric response measurement. To this end, the measured values for the permittivity ε' and loss tangent $\tan(\delta)$ in the frequency range from 0.220 THz to 0.325 THz were imported into CST Microwave Studio and fitted using a dispersion model of first order.

2. Design of MCFS-based THz structures

The functionality and characteristics of the MCFS-based THz structures crucially rely on the 3D-printed polymeric support structures and the associated isolation trenches with undercut sidewalls, see Section 2 and Fig. 2b of the main manuscript. A cross-sectional view of a typical MCFS is shown in Fig. S2a, where the indicated dimensions refer to TIC II, see Section 3 and associated discussion in the Materials and Methods Section of the main manuscript. The MCFS consists of the 3D-printed polymeric support ($\varepsilon' = 2.66$, $\tan(\delta) = 0.033$) on an alumina substrate ($\varepsilon' = 9.9$, $\tan(\delta) = 0.0001$) and is locally coated through highly directive metal deposition along a direction perpendicular to the substrate, i.e., from top along the negative *z*-direction in Fig. S2a. The metal layer of thickness $h_m = 0.64\,\mu m$ is thus deposited on all surfaces with direct line of sight to the evaporation source, thereby forming three isolated metal strips that represent the ground-signal-ground (GSG) transmission line, see also Fig. 2d of the main manuscript. For a robust design, the depth d_{it} of the isolation trenches should be chosen large enough to avoid any influence of the unavoidable metal residues at the ground of the trenches on the electrical characteristics of the TIC, in particular the line impedance. This aspect is investigated in more detail in Fig. S2b, which depicts the simulated line impedance Z_L as a function of the gap width w_{gap} and the isolation-trench depth d_{it}. In these simulations, the support height was chosen to be $h = 100\,\mu m$, which is large enough to avoid any influence of the high-permittivity substrate on the results. Contour lines in Fig. S2b indicate the set of parameters that lead to constant line impedances $Z_L = (50...80)\,\Omega$. As expected, the line impedance can be effectively controlled by adapting the gap width w_{gap}, whereas the influence of the isolation-trench depth d_{it} is rather small once d_{it} exceeds twice the gap width w_{gap}, $d_{it} > 2w_{gap}$, i.e., to the right of the dashed white line in Fig. S2b. In our experiments, all fabricated support structures were thus designed with isolation-trench depths d_{it} of 20 µm or more, and we rely on the gap width w_{gap} to control the line impedance Z_L. Still, the transition section between the CPW and the MCFS requires special consideration, since the

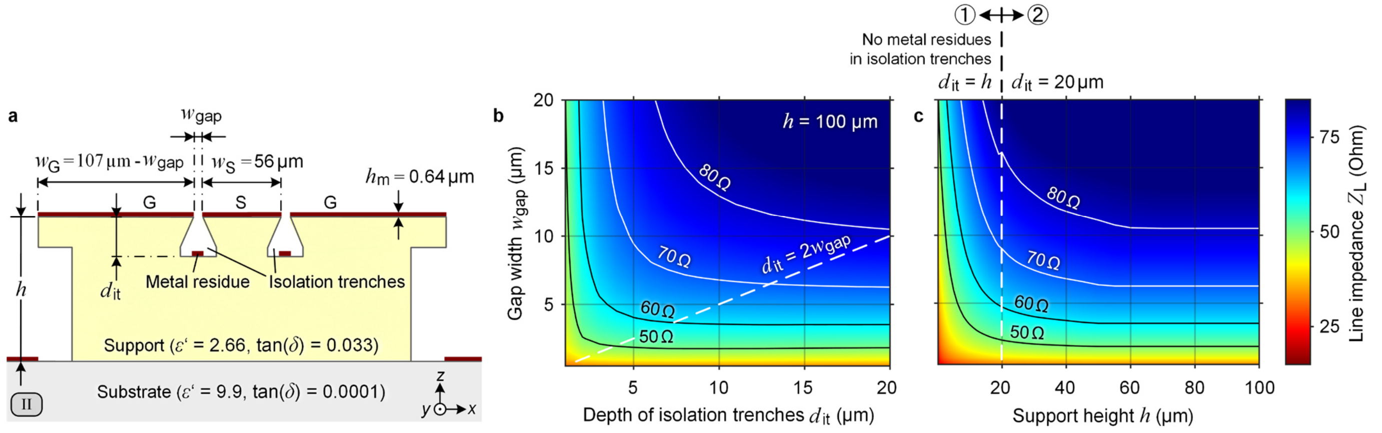

Fig. S2 | Simulation of characteristic line impedance for MCFS-based THz structures and design of the transition to an on-chip CPW. **a** Cross-sectional view of a transmission line on a typical MCFS. The MCFS consists of the 3D-printed polymeric support on an alumina substrate and is locally coated through highly directive metal evaporation along a direction perpendicular to the substrate, i.e., from top along the negative *z*-direction. The metal layer is thus deposited on all surfaces with direct line of sight to the evaporation source, thereby forming the three isolated metal strips in ground-signal-ground (GSG) configuration. For a robust design, the depth d_{it} of the isolation trenches should be chosen large enough to avoid any influence of the metal residues at the ground of the trenches on the electrical characteristics such as the line impedance of the TIC. Still, the transition section between the CPW and the MCFS requires special consideration, since the height h of the support structure is continuously tapered down to ensure a smooth connection to the approximately 3 µm-thick CPW strips on the substrate and since the isolation-trench depth d_{it} cannot exceed the support height h. To avoid formation of shortcuts, deposition of metal in the tapered region of the isolation trenches is avoided by dedicated shadowing structures that take the form of multiple arm-like roofs, see Inset 2 of Fig. 2c in the main manuscript. **b** Simulated line impedance Z_L as a function of the gap width w_{gap} and the isolation-trench depth d_{it}. The support height was chosen to be $h = 100\,\mu m$ – large enough to avoid any influence of the high-permittivity substrate on the results. Contour lines indicate the set of parameters for constant line impedances of $Z_L = (50...80)\,\Omega$. As expected, the line impedance can be effectively controlled by adapting the gap width w_{gap}, whereas the influence of the isolation-trench depth d_{it} is rather small once d_{it} exceeds twice the gap width w_{gap}, $d_{it} > 2w_{gap}$, i.e., to the lower right of the dashed white line. In our experiments, all fabricated support structures were thus designed with $d_{it} \geq 20\,\mu m$, and we rely on the gap width w_{gap} to control the line impedance. **c** For correct choice of the gap width in the transition region, we simulate again the line impedance Z_L as a function of the gap width w_{gap} and the support height h, now subdividing the simulation in two distinct regions, labeled ① and ②: For large support heights $h > 20\,\mu m$, the isolation-trench depth d_{it} is fixed to 20 µm, and metal residues are present at the ground of the isolation trenches (Region ②). In the transition region between the CPW and the MCFS, the support height h is smaller than 20 µm, the isolation-trench depth is equal to the support height, $d_{it} = h$, and the trenches do not contain any metal residues (Region ①) due to the above-mentioned shadowing structures. In all simulations, we kept the signal-conductor width w_S fixed and varied the ground-conductor width w_G such that the overall structure width is maintained at a constant total width of $w_S + 2w_G + 2w_{gap} = 270\,\mu m$. This allows for geometrically smooth and electrically well-matched transitions to the fabricated CPW feeds, which also feature a total width of $w_S + 2w_G + 2d_{SG} = 270\,\mu m$ for TIC II. Contour lines again indicate constant line impedances of $Z_L = (50...80)\,\Omega$. For the 80 Ω contour line, we observe a small discontinuity at the transition between Region ① and Region ②. We attribute this to the fact that, due to the associated rather large gap width of the order of 15 µm, the abrupt stop of the metal residues on the ground of the isolation trenches still has a slight influence on the resulting line impedance.

height h of the support structure is continuously tapered down from an initial value of typically 50 µm or more to approximately 3 µm to ensure a smooth connection to the approximately 3 µm-thick CPW strips on the substrate, see Fig. 2f of the main manuscript. At the same time, the isolation-trench depth d_{it} cannot exceed the support height h and must hence be down-tapered as well – from the initial 20 µm or more to approximately 3 µm. To avoid formation of shortcuts, deposition of metal in the tapered region of the isolation trench is avoided by dedicated shadowing structures that have the form of multiple arm-like roofs, see Inset 2 of Fig. 2c in the main manuscript. For correct choice of the gap width in this transition region, we simulate again the line impedance Z_L as a function of that gap width w_{gap} and the support height h, see Fig. S2c. In this simulation, we consider two distinct regions, labelled ① and ②: For large support heights $h > 20\,\mu m$, the isolation-trench depth d_{it} is fixed to 20 µm, and metal residues are present at the ground of the isolation trenches, see Region ② in Fig. S2c. In the transition region between the CPW and the MCFS, the isolation-trench depth is equal to the support height, $d_{it} = h$, and the trenches do not contain any metal residues since deposition is prevented by the shadowing structures, see Region ① in Fig. S2c. In all simulations, we kept the signal-conductor width w_S fixed and varied the ground-conductor width w_G such that the overall structure width is maintained at a constant total width of $w_S + 2w_G + 2w_{gap} = 270\,\mu m$. This allows for geometrically smooth and electrically well-matched transitions to the fabricated CPW feeds, which also feature a total width of $w_S + 2w_G + 2d_{SG} = 270\,\mu m$ for TIC II, see Fig. 2a and Table 1 along with the associated explanation in the Methods section in the main manuscript. Contour lines in Fig. S2c again indicate constant line impedances of $Z_L = (50...80)\,\Omega$. For the 80 Ω contour line, we observe a small discontinuity at the transition between Region ① and Region ②. We attribute this to the fact that, for the associated rather large gap width of the order of 15 µm, the abrupt stop of the metal residues on the ground of the 20 µm deep isolation trenches still has a slight influence on the resulting line impedance. Note that for some of the structures discussed in the main manuscript, the adjustment of the gap width w_{gap} was not yet implemented to provide a perfectly smooth transition, see, e.g., Fig. 3b of the main manuscript. This leaves room for further optimization and improvement of the overall device performance.

3. Surface roughness measurements

The surface roughness of the various fabricated MCFS and of the feed CPW was measured using a white-light interferometer (ContourX-100, Bruker Inc., Billerica, USA) equipped with a 100× / 0.8 objective (WLI100XMRTC, Olympus K.K., Tokyo, Japan). The results are shown in Fig. S3 . All measurements are performed in $(40\times40)\,\mu\mathrm{m}^2$ fields, averaging over ten recordings for each field to reduce noise, and we apply a software-based tilt correction followed by a background subtraction to compensate for the waviness of the sampled areas. Final roughness extraction consisted of separating the measured height profile in a series of single-line profiles for which the mean root-mean-square (RMS) roughness R_q is computed[9]. Moreover, different fields on multiple positions have been measured for each sample to reliably determine the RMS surface roughness and its typical range of variation across the sample.

In Fig. S3 a, the height deviations Δz from the mean surface profile are shown for an exemplary bare 3D-printed support structure (left panel) and for the same structure after the metal coating process (right panel). The various measurements reveal an RMS surface roughness of $R_\mathrm{q,MCFS}=(13...14)\,\mathrm{nm}$ upon metal deposition, which is slightly larger than the roughness of the underlying 3D-printed support of $R_\mathrm{q,support}=(9...10)\,\mathrm{nm}$. We also evaluated the surface roughness of the gold metallization on the alumina substrates used for fabrication of the CPW transmission lines in our experiments, Fig. S3 b. We found a rather large RMS surface roughness of $R_\mathrm{q,gold}=(121...129)\,\mathrm{nm}$, which was subsequently included in the simulations of the transmission lines, see Methods section of the main manuscript.

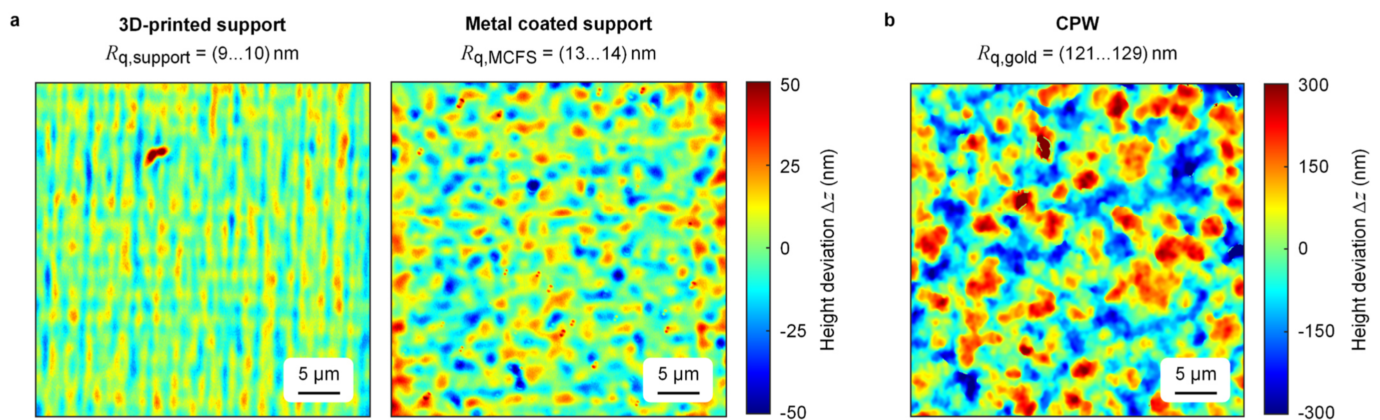

Fig. S3 | Surface topographies and associated surface roughness extracted from white-light interferometer measurements. **a** Height deviations Δz from the mean surface profile for an exemplary bare 3D-printed support structure (left panel) and for the same structure after the metal coating process (right panel). A root-mean-square (RMS) surface roughness of $R_\mathrm{q,MCFS}=(13...14)\,\mathrm{nm}$ is found after metal deposition, slightly larger than the roughness of the underlying 3D-printed support of $R_\mathrm{q,support}=(9...10)\,\mathrm{nm}$. **b** Height deviations Δz measured for the gold metallization on the alumina substrates used for fabrication of the CPW transmission lines in our experiments. We found a rather large RMS surface roughness of $R_\mathrm{q,gold}=(121...129)\,\mathrm{nm}$.

4. Influence of metal conductivity

To quantify the influence of the conductivity of the deposited metal on the performance of the resulting MCFS, we exemplarily simulate the transmission of the second THz interconnect (TIC II, see Section "THz interconnects (TIC)" of the main manuscript) with varying levels of conductivity. In these simulations, the conductivity of the metal layer is set to 1 %, 10 % and 100 % of the benchmark conductivity of copper as defined by the International Annealed Copper Standard (IACS, $\sigma_\mathrm{IACS}=5.8\times10^7\,\mathrm{S/m}$), and the associated transmission $S_{21,\mathrm{dB}}=10\log_{10}(|\underline{S}_{21}|^2)$ for TIC II is calculated, see red, blue and green traces in Fig. S4, respectively. The dashed black line in Fig. S4 indicates the simulated transmission for a metal conductivity of $\sigma_\mathrm{MCFS}=3.29\times10^7\,\mathrm{S/m}$, corresponding to 57% of the IACS benchmark, as measured for our MCFS, see "Materials and Methods" Section of the main manuscript. In all of these simulations, the total thickness of the metal layer was set to $h_\mathrm{m}=0.64\,\mu\mathrm{m}$, in accordance with the manufactured TIC, and we also include the measured RMS surface roughness $R_\mathrm{q,MCFS}=(13\ldots14)\,\mathrm{nm}$, see previous Section "3. Surface roughness measurements" for details. From our simulations, we find that the transmission of TIC II can only be improved by less than 0.1 dB when increasing the conductivity from that of our current structures (57 % IACS) to that of ideal bulk copper (100 % IACS). More specifically, at a frequency of 200 GHz, the simulated total loss of the 0.5 mm-long interconnect would amount to 0.53 dB (1.06 dB/mm) when assuming ideal copper (100 % IACS) – only slightly lower than the loss of 0.54 dB (1.08 dB/mm) obtained for the current structures (57 % IACS). Although the performance of the device starts to degrade to a notable degree if the conductivity falls below 10 % of the IACS benchmark, the simulated transmission loss still remains below 1 dB up to 230 GHz with 3 dB-bandwidths only slightly reducing, see blue curve in Fig. S4 below. In this case, the simulated total loss amounts to 0.83 dB (1.66 dB/mm) at 200 GHz. More significant performance degradations are found for a conductivity equivalent to 1 % of the IACS benchmark, see red curve in Fig. S4. In this case, the simulated transmission $S_{21,\mathrm{dB}}$ of TIC II drops by 0.9 dB for

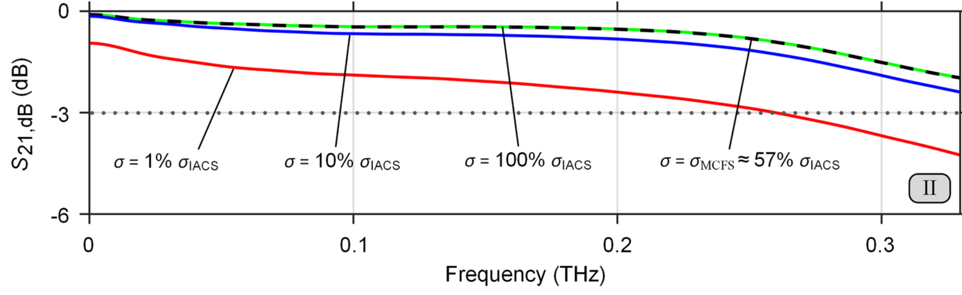

Fig. S4 | Simulation of the transmission of THz interconnect II (TIC II) for varying levels of the metal conductivity with respect to the IACS bulk-copper benchmark ($\sigma_{IACS} = 5.8 \times 10^7$ S/m). For our current MCFS, the conductivity of the metal layer amounts to 57 % of the IACS benchmark, $\sigma = \sigma_{MCFS} = 0.57\ \sigma_{IACS}$, leading already to outstanding transmission performance (dashed black trace) that is essentially indistinguishable from that obtained for ideal copper (100 % IACS). More specifically, the transmission of the current TIC II can only be further improved by less than 0.1 dB if a conductivity equivalent to 100 % of the IACS benchmark could be reached, $\sigma = \sigma_{IACS}$ (green curve). In both cases, the overall losses of the TIC seem to be dominated by dielectric losses, scattering from surface roughness and radiation. Severe performance degradations only occur for conductivities of the metal layers below 10 % of the IACS benchmark ($\sigma = 0.1\ \sigma_{IACS}$ and $\sigma = 0.01\ \sigma_{IACS}$).

frequencies approaching DC, while for higher frequencies the loss increases even further. At a frequency of 200 GHz, the simulated total loss is 2.40 dB (4.80 dB/mm). These results are in line with the expectation that the conductor loss scales inversely with $1/\sqrt{\sigma}$ for metal layer thicknesses being a multiple of the skin depth at the associated operating frequency[10]. We hence conclude that further increasing the bulk conductivity of the deposited metal layers would have limited impact on the performance of the rather fine and small structures demonstrated in our work and that the concept is also compatible with other metals that are widely established in microfabrication, comprising, e.g., aluminum (Al, $\sigma_{Al} = 0.61\ \sigma_{IACS}$), gold (Au, $\sigma_{Au} = 0.70\ \sigma_{IACS}$), silver (Ag, $\sigma_{Ag} = 1.05\ \sigma_{IACS}$), or nickel (Ni, $\sigma_{Ni} = 0.25\ \sigma_{IACS}$), see Section "RF losses and potential for performance improvement" of the main manuscript.

5. Characterization of THz interconnects (TIC)

The TIC were measured on a semi-automated probing station (Summit 12000B-S, Cascade Microtech Inc., Beaverton, USA), enabling repeatable and consistent contacting of the samples under test. For *S*-parameter measurements in the different frequency ranges, a VNA (N5247B PNA-X, Keysight Technologies Inc., Santa Rosa, USA) is used in conjunction with a pair of frequency-extending transmit / receive modules connected via a millimeter-wave controller (N5262A, Keysight Technologies Inc.). The VNA is set to measure at 801 frequency points with an IF bandwidth of 100 Hz for all recordings.

For the measurements shown in Fig. 3c and d of the main manuscript, a total of three frequency ranges (10 MHz … 0.110 THz; 0.110 THz … 0.170 THz; 0.200 THz … 0.330 THz) are addressed by selecting the associated extension modules and probes, and a line-reflect-reflect-match (LRRM) calibration[11] was carried out using the manufacturer-recommended impedance-standard substrate (ISS) to shift the reference planes to the probe tips. All measurements are done on a microwave-absorbing ISS holder (116-344, FormFactor GmbH, Thiendorf, Germany) to reduce unwanted substrate modes. For the frequency range from 10 MHz to 0.110 THz, we use a first pair of frequency-extension modules (N5260-60003, Keysight Technologies Inc.) and coaxial probes (Infinity Probe i110-A-GSG-100, FormFactor GmbH), and the LRRM calibration is performed on the associated ISS (104-783, FormFactor GmbH). The second frequency range from 0.110 THz to 0.170 THz is measured with a second pair of frequency-extension modules (V06VNA2-T/R-A, OML Inc.) and waveguide probes (Infinity Probe i170-T-GSG-100-BT, FormFactor GmbH). Lastly, measurements in the third frequency range from 0.200 THz to 0.330 THz are carried out with a third pair of frequency-extension modules (V03VNA2-T/R-A, OML Inc.) and waveguide probes (Infinity Probe i325-T-GSG-100-BT, FormFactor GmbH). The LRRM calibrations for the measurements in the latter two frequency ranges are performed on a second ISS (138-357, FormFactor GmbH).

The measured *S*-parameter matrices $\underline{\mathbf{S}}_{\mathrm{meas}}$ between Plane $1'$ and Plane $2'$ (blue lines in Fig. 3a of the main manuscript) comprise the compound characteristics of the respective TIC (TIC I, II, and III) as well as of the two associated 4 mm-long CPW feeds on the alumina substrates. The measured frequency-dependent loss is thus largely dominated by the loss of the two CPW feeds, and we need to mathematically remove their influence via dedicated de-embedding procedures[12]. To this end, the compound *S*-parameter matrices $\underline{\mathbf{S}}_{\mathrm{meas}}$ are first transformed into transfer matrices (*T*-matrices[10], see Supplementary Section 8), and the *T*-matrix $\underline{\mathbf{T}}_{\mathrm{meas}}$ of the network is subsequently represented by cascading the *T*-matrices of the individual elements,

$$\underline{\mathbf{T}}_{\mathrm{meas}} = \underline{\mathbf{T}}_{\mathrm{feed}}\,\underline{\mathbf{T}}_{\mathrm{TIC}}\,\underline{\mathbf{T}}_{\mathrm{feed}}\,. \tag{1}$$

In this relation $\underline{\mathbf{T}}_{\mathrm{feed}}$ and $\underline{\mathbf{T}}_{\mathrm{TIC}}$ represent the *T*-matrices of the two identical CPW feeds and the corresponding TIC, respectively. We then measured the *S*-parameter matrix $\underline{\mathbf{S}}_{\mathrm{feed,ref}}$ of an identical reference CPW with the length L_{feed}

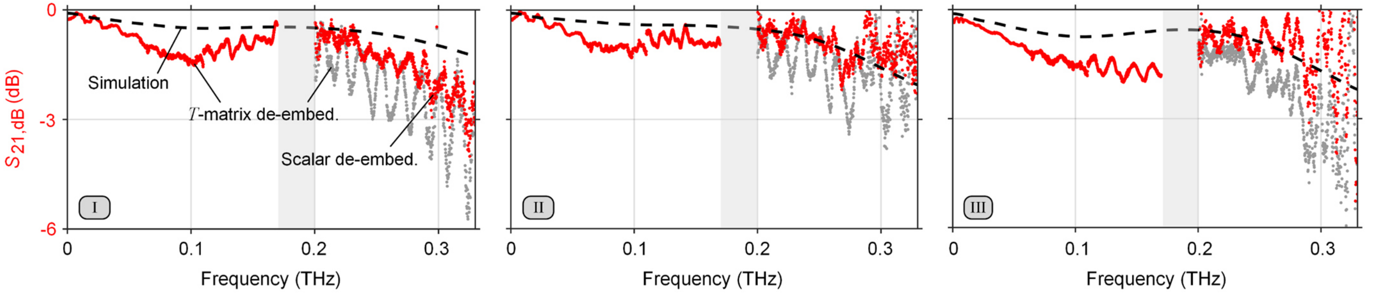

Fig. S5 | De-embedding of THz interconnects (TIC) using the *T*-matrix and the scalar de-embedding approach. In our measurements of the TIC structure, the recorded *S*-parameter matrices do not only comprise the characteristics of the TIC, but also those of the two 4 mm-long CPW feeds on the two alumina substrates, which may dominate the overall transmission characteristics. For frequencies below 0.170 THz, the feed lines feature low transmission losses and are well matched such that a mathematically rigorous *T*-matrix de-embedding technique according to Eq. (2) can be used. In this frequency range, the associated transmission $S_{21,\mathrm{dB}} = 10\log_{10}(|\underline{S}_{21}|^2)$ is indicated by red curves for TIC I (left), II (middle), and III (right). For frequencies beyond 0.200 THz, the feed lines become lossy and poorly matched, rendering the results of the *T*-matrix de-embedding technique unreliable and leading to strong oscillations of the associated curves, which are indicated in grey. We therefore resort to a simpler and more robust scalar correction approach as given in Eq. (4) for estimating the TIC transmission in the frequency range from 0.200 THz to 0.330 THz. The results are again indicated by red curves in this frequency range, exhibiting less fluctuations than the results obtained from the *T*-matrix approach. Note that the measured *S*-parameters had to be acquired separately in different frequency ranges using dedicated signal sources, waveguides, and probes as described above, thereby leaving a gap between 0.170 THz and 0.200 THz, where no adequate signal sources were available.

and calculated the corresponding *T*-matrix $\underline{\mathbf{T}}_{\mathrm{feed,ref}}$. Equation (1) can then be multiplied from both sides by the inverse matrix $\underline{\mathbf{T}}^{-1}_{\mathrm{feed,ref}}$, leading to

$$\underline{\mathbf{T}}^{-1}_{\mathrm{feed,ref}}\,\underline{\mathbf{T}}_{\mathrm{meas}}\,\underline{\mathbf{T}}^{-1}_{\mathrm{feed,ref}} = \underline{\mathbf{T}}^{-1}_{\mathrm{feed,ref}}\,\underline{\mathbf{T}}_{\mathrm{feed}}\,\underline{\mathbf{T}}_{\mathrm{TIC}}\,\underline{\mathbf{T}}_{\mathrm{feed}}\,\underline{\mathbf{T}}^{-1}_{\mathrm{feed,ref}} = \underline{\mathbf{T}}_{\mathrm{TIC}}\,. \tag{2}$$

In this relation, we have made the assumption that the *T*-matrix of the CPW embedded in the measurement $\underline{\mathbf{T}}_{\mathrm{feed}}$ and of the separately measured reference CPW $\underline{\mathbf{T}}_{\mathrm{feed,ref}}$ are identical, i.e., $\underline{\mathbf{T}}^{-1}_{\mathrm{feed,ref}}\,\underline{\mathbf{T}}_{\mathrm{feed}} = \underline{\mathbf{T}}_{\mathrm{feed}}\,\underline{\mathbf{T}}^{-1}_{\mathrm{feed,ref}} = \mathbf{I}$, where $\mathbf{I}$ denotes the unity matrix. The extracted *T*-matrix $\underline{\mathbf{T}}_{\mathrm{TIC}}$ can then be converted back to the *S*-parameter matrix $\underline{\mathbf{S}}_{\mathrm{TIC}}$ with its complex transmission and reflection coefficients $\underline{S}_{21}$ and $\underline{S}_{11}$, respectively. Figure S5 shows the resulting transmission factor $S_{21,\mathrm{dB}} = 10\log_{10}(|\underline{S}_{21}|^2)$ of TIC I (left), II (middle), and III (right) as extracted via the *T*-matrix de-embedding approach described in Eq. (2) as red curves in the frequency range up to 0.170 THz. For frequencies beyond 0.200 THz, we find increasingly strong ripples in the de-embedded data, that are caused by error multiplication arising from slight discrepancies between the “true” *T*-matrix $\underline{\mathbf{T}}_{\mathrm{feed}}$ of the CPW feed lines and its experimentally measured counterpart $\underline{\mathbf{T}}_{\mathrm{feed,ref}}$ – a known effect in mm-wave device characterization[13]. This leads to a high sensitivity of the de-embedding procedure with respect to the insertion and return loss of the reference CPW and renders the results unreliable for frequencies beyond 0.200 THz, see next paragraph for a more detailed explanation. As mentioned in the main manuscript, we therefore rely on a more robust scalar correction rather than on a mathematically rigorous but experimentally sensitive *T*-matrix de-embedding. For comparison of both approaches, we still display the results of the *T*-matrix de-embedding beyond 0.200 THz in Fig. S5, see grey curves. Note that the measured *S*-parameters had to be acquired separately in different frequency ranges using dedicated signal sources, waveguides, and probes as described above. This leaves a gap between 0.170 THz and 0.200 THz, where no adequate signal sources were available.

In the following, we aim at obtaining a better understanding of the effects of error multiplication in the *T*-matrix de-embedding approach. To this end, we distinguish between the “true” *T*-matrix $\underline{\mathbf{T}}_{\mathrm{feed}}$ of the CPW as contained in the measured compound *T*-matrix $\underline{\mathbf{T}}_{\mathrm{meas}}$ and of the separately measured reference CPW $\underline{\mathbf{T}}_{\mathrm{feed,ref}}$ which differ from one another due to measurement inaccuracies, $\underline{\mathbf{T}}_{\mathrm{feed}} \neq \underline{\mathbf{T}}_{\mathrm{feed,ref}}$. The matrix multiplications $\underline{\mathbf{T}}^{-1}_{\mathrm{feed,ref}}\,\underline{\mathbf{T}}_{\mathrm{feed}}$ and $\underline{\mathbf{T}}_{\mathrm{feed}}\,\underline{\mathbf{T}}^{-1}_{\mathrm{feed,ref}}$ in Eq. (2) are therefore no longer given by the unity matrix $\mathbf{I}$ and thus introduce errors during the de-embedding procedure. As an example, the first matrix multiplication in Eq. (2) can be written in terms of the underlying *S*-parameters as

$$\begin{aligned}
\underline{\mathbf{T}}^{-1}_{\mathrm{feed,ref}}\,\underline{\mathbf{T}}_{\mathrm{feed}} &= \begin{pmatrix} 1\big/\underline{S}_{21}^{\mathrm{feed,ref}} & -\underline{S}_{22}^{\mathrm{feed,ref}}\big/\underline{S}_{21}^{\mathrm{feed,ref}} \\ \underline{S}_{11}^{\mathrm{feed,ref}}\big/\underline{S}_{21}^{\mathrm{feed,ref}} & [(\underline{S}_{21}^{\mathrm{feed,ref}})^2 - \underline{S}_{11}^{\mathrm{feed,ref}}\underline{S}_{22}^{\mathrm{feed,ref}}]\big/\underline{S}_{21}^{\mathrm{feed,ref}} \end{pmatrix}^{-1} \begin{pmatrix} 1\big/\underline{S}_{21}^{\mathrm{feed}} & -\underline{S}_{22}^{\mathrm{feed}}\big/\underline{S}_{21}^{\mathrm{feed}} \\ \underline{S}_{11}^{\mathrm{feed}}\big/\underline{S}_{21}^{\mathrm{feed}} & [(\underline{S}_{21}^{\mathrm{feed}})^2 - \underline{S}_{11}^{\mathrm{feed}}\underline{S}_{22}^{\mathrm{feed}}]\big/\underline{S}_{21}^{\mathrm{feed}} \end{pmatrix} \\
&= \begin{pmatrix} \dfrac{\underline{S}_{21}^{\mathrm{feed,ref}}}{\underline{S}_{21}^{\mathrm{feed}}} + \dfrac{\underline{S}_{22}^{\mathrm{feed,ref}}}{\underline{S}_{21}^{\mathrm{feed}}\underline{S}_{21}^{\mathrm{feed,ref}}}\left(\underline{S}_{11}^{\mathrm{feed}} - \underline{S}_{11}^{\mathrm{feed,ref}}\right) & \left(\dfrac{\underline{S}_{21}^{\mathrm{feed}}\underline{S}_{22}^{\mathrm{feed,ref}}}{\underline{S}_{21}^{\mathrm{feed,ref}}} - \dfrac{\underline{S}_{21}^{\mathrm{feed,ref}}\underline{S}_{22}^{\mathrm{feed}}}{\underline{S}_{21}^{\mathrm{feed}}}\right) - \dfrac{\underline{S}_{22}^{\mathrm{feed}}\underline{S}_{22}^{\mathrm{feed,ref}}}{\underline{S}_{21}^{\mathrm{feed}}\underline{S}_{21}^{\mathrm{feed,ref}}}\left(\underline{S}_{11}^{\mathrm{feed}} - \underline{S}_{11}^{\mathrm{feed,ref}}\right) \\ \dfrac{1}{\underline{S}_{21}^{\mathrm{feed}}\underline{S}_{21}^{\mathrm{feed,ref}}}\left(\underline{S}_{11}^{\mathrm{feed}} - \underline{S}_{11}^{\mathrm{feed,ref}}\right) & \dfrac{\underline{S}_{21}^{\mathrm{feed}}}{\underline{S}_{21}^{\mathrm{feed,ref}}} - \dfrac{\underline{S}_{22}^{\mathrm{feed}}}{\underline{S}_{21}^{\mathrm{feed}}\underline{S}_{21}^{\mathrm{feed,ref}}}\left(\underline{S}_{11}^{\mathrm{feed}} - \underline{S}_{11}^{\mathrm{feed,ref}}\right) \end{pmatrix}.
\end{aligned} \tag{3}$$

In this relation, we denote the various *S*-parameters of the "true" embedded CPW and the separately measured reference CPW by the superscripts "feed" and "feed,ref", respectively, and we assumed all systems to be reciprocal, i.e., $\underline{S}_{21}^{\text{feed}} = \underline{S}_{12}^{\text{feed}}$ and $\underline{S}_{21}^{\text{feed,ref}} = \underline{S}_{12}^{\text{feed,ref}}$. For an ideal measurement without noise, the underlying scattering parameters of $\underline{\mathbf{T}}_{\text{feed}}$ and $\underline{\mathbf{T}}_{\text{feed,ref}}$ are identical, i.e., $\underline{S}_{lm}^{\text{feed}} = \underline{S}_{lm}^{\text{feed,ref}}$ with $l,m \in \{1,2\}$, and the multiplication of the associated *T*-matrices in Eq. (3) leads to the unity matrix $\mathbf{I}$ as assumed for deriving the de-embedding procedure in Eq. (2). For noisy measurements, however, the expressions indicated in blue in Eq. (3) can become very big, given the fact that, for large frequencies, the feed lines become increasingly lossy and reflective. As a consequence, the products $\underline{S}_{21}^{\text{feed,ref}} \underline{S}_{21}^{\text{feed}}$ in the denominator of the highlighted expressions become small, while the numerators are either unity or increase with the reflection coefficients $\underline{S}_{22}^{\text{feed}}$, $\underline{S}_{22}^{\text{feed,ref}}$ and $\underline{S}_{22}^{\text{feed}} \underline{S}_{22}^{\text{feed,ref}}$. This leads to large values of the overall fraction which strongly "amplifies" any noise- or distortion-induced deviations[13] between the reflection $\underline{S}_{11}^{\text{feed}}$ of the "true" feed line and its measured counterpart $\underline{S}_{11}^{\text{feed,ref}}$. In our measurements, these effects are particularly detrimental for frequencies above 0.200 THz, indicated by the strong oscillations of the grey traces in Fig. S5.

To mitigate this problem, we use a more robust scalar correction technique to estimate the loss of the TIC for frequencies above 0.200 THz, effectively removing only the attenuation of the CPW feeds from the recorded measurements between Plane $1'$ and Plane $2'$. More specifically, we first extract the transmission of the full arrangement $S_{2'1',\text{meas,dB}} = 10\log_{10}(|\underline{S}_{2'1',\text{meas,dB}}|^2)$ from the measured compound *S*-parameter matrix $\underline{\mathbf{S}}_{\text{meas}}$, and we obtain the transmission $S_{2'1',\text{ref,dB}} = 10\log_{10}(|\underline{S}_{2'1',\text{ref}}|^2)$ of one 4 mm-long CPW feed from the separately measured *S*-parameter matrix $\underline{\mathbf{S}}_{\text{feed,ref}}$. Finally, the loss of the two feed lines is removed from the compound measurement by subtracting the associated dB-values,

$$S_{21,\text{dB}} = S_{2'1',\text{meas,dB}} - 2S_{2'1',\text{ref,dB}}. \tag{4}$$

The transmission factor $S_{21,\text{dB}}$ of TIC I (left), II (middle), and III (right) extracted via the scalar correction according to Eq. (4) was calculated for frequencies between 0.200 THz and 0.330 THz, see red curves in Fig. S5. As expected, the data appears to fluctuate much less than the results obtained from the *T*-matrix approach that are indicated by the grey traces above 0.200 THz. Notably, the results of both techniques are reasonably consistent at lower frequencies close to 0.200 THz, supporting the validity of the approach.

Clearly, the scalar correction technique does not account for the reflection coefficients of the feeds and the TIC and further suffers from deviations between the *S*-parameters that were separately measured for the reference CPW and their "true" counterparts that are effective in the measurement of the *S*-parameters between Plane $1'$ and Plane $2'$. To quantitatively assess the inaccuracy introduced by these approximations and measurement inaccuracies, we performed a Monte-Carlo analysis using the second THz interconnect (TIC II) as an exemplary device under test (DUT), see Section "THz interconnects (TIC)" of the main manuscript. We consider the frequency range between 0.200 THz and 0.330 THz, which we discretize in steps of 1 GHz. For each of the frequency points, we simulate the transmission of the complete measurement chain (feed–DUT–feed) using reciprocal and symmetric two-port networks that are described by transfer matrices (*T*-matrices) as explained above, see Eq. (1). To perform these simulations, the full *T*-matrices of the DUT and the feeds need to be known. For the feeds, the initial *T*-matrices can be directly extracted from the *S*-parameters measured for a separate reference feed line. To account for the unavoidable errors of these measurements, we stochastically vary both the amplitude and the phase of the measured *S*-parameters as described in the next paragraph below. In contrast to the feeds, the transmission characteristics of the DUT are not directly accessible by measurements. We therefore extracted an estimate of the magnitude $|\underline{S}_{21,\text{in}}|$ of the DUT transmission parameter from the data obtained from the scalar de-embedding technique, using a polynomial fit of fifth order to suppress the pronounced frequency-dependent fringes. The phase of the complex-valued DUT transmission parameter $\underline{S}_{21,\text{in}}$ was not directly accessible, and we assumed a linear frequency dependence corresponding to a delay of 2 ps, coinciding with the delay found in the simulation of the TIC. Similarly, we could not rely on any measured data for the reflection characteristics $\underline{S}_{11,\text{in}}$ of the DUT and had to use the results of electromagnetic simulations. With the full *T*-matrices of the feeds and the DUT at hand, we simulate the transmission of the complete chain (feed–DUT–feed) and then use the scalar de-embedding approach to reconstruct the frequency-dependent power transmission factor $|\underline{S}_{21,\text{MC}}|^2$ obtained from the various Monte-Carlo simulations of the DUT. Due to the variations of the feed-line *S*-parameters, the result differs from the power transmission $|\underline{S}_{21,\text{in}}|^2$ that was initially used to simulate the complete chain. We can thus estimate the error $\Delta S_{21,\text{DUT,dB}} = S_{21,\text{MC,dB}} - S_{21,\text{in,dB}}$ between the associated dB-values $S_{21,\text{MC,dB}} = 10\log_{10}(|\underline{S}_{21,\text{MC}}|^2)$ and $S_{21,\text{in,dB}} = 10\log_{10}(|\underline{S}_{21,\text{in}}|^2)$, as introduced by the combined effect of uncertainties in the feed-line measurements and the intrinsic approximations of the scalar de-embedding technique.

The measurement uncertainties of the feed-line characteristics were extracted from an extensive study[14] of stochastic variations in *S*-parameter measurements in the frequency range between 0.220 THz and 0.325 THz, caused by, e.g., inaccurate probe placement and fabrication tolerances of transmission-line structures. According to this study, the standard deviation of the relative amplitude error amounts to $\Delta|\underline{S}_{21,\text{feed}}|/|\underline{S}_{21,\text{feed}}| = \Delta|\underline{S}_{12,\text{feed}}|/|\underline{S}_{12,\text{feed}}| = 3\ \%$ (0.3 dB) and the phase error is $\Delta\varphi_{21,\text{feed}} = \Delta\varphi_{12,\text{feed}} = 6°$, respectively. For the reflection

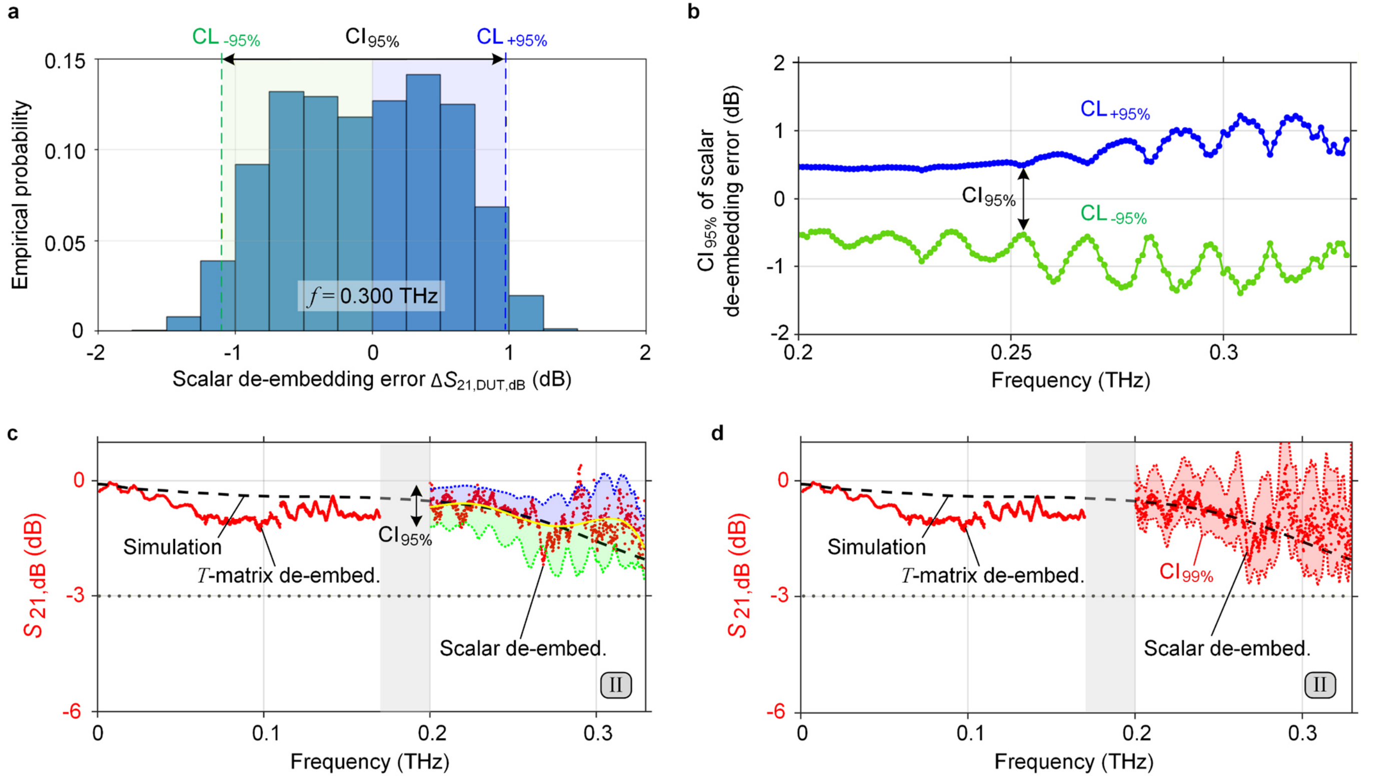

Fig. S6 | Monte-Carlo analysis of the scalar de-embedding error associated with the measurement of THz interconnect II (TIC II) above 0.200 THz. **a** Exemplary histogram of the scalar de-embedding error at a frequency of 0.300 THz. The horizontal axis indicates the de-embedding-related error $\Delta S_{21,\mathrm{DUT,dB}}$ of the transmission scattering parameter $S_{21,\mathrm{dB}}$, and the vertical axis indicates the empirical probability for a bin size of 0.25 dB. The green- and blue-shaded regions indicate the single-sided 95 % confidence intervals associated with the negative and positive deviations, bounded by the associated confidence levels $\mathrm{CL}_{-95\%}$ and $\mathrm{CL}_{+95\%}$, respectively. The area between these two confidence levels hence defines the region in which 95 % of the overall scalar de-embedding-related errors fall. **b** Variation of the confidence levels $\mathrm{CL}_{-95\%}$ and $\mathrm{CL}_{+95\%}$ and the associated (asymmetric) confidence interval $\mathrm{CI}_{95\%}$ within the frequency range from 0.200 THz to 0.330 THz. **c** Initially measured transmission of the DUT (red dots) along with the fifth-order polynomial fit in the frequency range from 0.200 THz to 0.330 THz (yellow line) used as an initial assumption $|\underline{S}_{21,\mathrm{in}}|$ for the Monte-Carlo simulations. The confidence region associated with the asymmetric confidence interval of total width $\mathrm{CI}_{95\%}(f)$ is shaded in green and blue below and above the polynomial line-fit, respectively. Note that 42 out of the total of 801 measured frequency points fall outside the region depicted by $\mathrm{CI}_{95\%}(f)$, therefore counting as outliers according to our Monte-Carlo simulation. This corresponds to 5.2 % of the total data points, which is in accordance with the confidence interval definition. **d** Range of true DUT power-transmission values, estimated from the 99 % confidence intervals of the positive and negative de-embedding-related error. We start from the measured DUT transmission that was obtained by the scalar de-embedding technique and subtract the expected de-embedding-related error as obtained from our Monte-Carlo simulation. The bound associated with the 99 % confidence interval of the true DUT values is indicated by the red-shaded region. Note that, despite significant measurement inaccuracies of the feed lines and the various underlying assumptions of our Monte-Carlo simulation, the resulting uncertainty of the DUT transmission remains within acceptable error bounds, confirming the notion that the scalar de-embedding approach is a pragmatic approximation.

factor $\underline{S}_{11,\mathrm{feed}}$, the study reports an absolute amplitude error of $\Delta|\underline{S}_{11,\mathrm{feed}}| = \Delta|\underline{S}_{22,\mathrm{feed}}| = 0.05$ and a phase error of $\Delta\varphi_{11,\mathrm{feed}} = \Delta\varphi_{22,\mathrm{feed}} = 12°$. For the Monte-Carlo simulations, we vary all eight input parameters, i.e., the amplitude and phase of each $\underline{S}_{21,\mathrm{feed}} = \underline{S}_{12,\mathrm{feed}}$ and $\underline{S}_{11,\mathrm{feed}} = \underline{S}_{22,\mathrm{feed}}$ for each of the two feed lines, assuming uniform distributions with standard deviations that correspond to the ones reported in the study[14], and we run a total of $N = 10^6$ iterations at each frequency point. For each simulation, we calculate the dB-value of the resulting de-embedding error, $\Delta S_{21,\mathrm{DUT,dB}} = S_{21,\mathrm{MC,dB}} - S_{21,\mathrm{in,dB}}$. The results of this analysis are summarized in Fig. S6. Figure S6a shows an exemplary histogram of the de-embedding error $\Delta S_{21,\mathrm{DUT,dB}}$ at a frequency of 0.300 THz. The horizontal axis indicates the de-embedding-related error $\Delta S_{21,\mathrm{DUT,dB}}$ of the transmission scattering parameter $S_{21,\mathrm{dB}}$, and the vertical axis indicates the empirical probability for a bin size of 0.25 dB, i.e., the share of error occurrences obtained from the Monte-Carlo simulation that fall into the respective bin. Note that, due to the nonlinear nature of the underlying model comprising, e.g., a magnitude-square operator and a logarithm in the expressions $S_{21,\mathrm{MC,dB}} = 10\log_{10}(|\underline{S}_{21,\mathrm{MC}}|^2)$ and $S_{21,\mathrm{in,dB}} = 10\log_{10}(|\underline{S}_{21,\mathrm{in}}|^2)$, the resulting error distribution is not symmetric with respect to $\Delta S_{21,\mathrm{DUT,dB}} = 0$. The green-shaded region in Fig. S6a indicates the single-sided 95 % confidence interval associated with the negative deviations, whereas the blue-shaded region indicates the single-sided 95 % confidence interval associated with values of positive deviations. The respective confidence levels (CL) are indicated by a green and blue dashed line and amount to $\mathrm{CL}_{-95\%}(0.300\ \mathrm{THz}) = -1.09$ dB and $\mathrm{CL}_{+95\%}(0.300\ \mathrm{THz}) = 0.98$ dB, respectively. The area between these two confidence levels hence defines the region in which 95% of the overall scalar de-embedding-related errors fall, i.e., the asymmetric confidence interval $\mathrm{CI}_{95\%}$. Figure S6b shows the variation of the confidence levels $\mathrm{CL}_{-95\%}$ and $\mathrm{CL}_{+95\%}$ and the associated confidence interval $\mathrm{CI}_{95\%}$ within the frequency range from 0.200 THz to 0.330 THz, exhibiting periodic variations that stem from fringes in the measured feed-line reflection coefficient. Figure S6c shows the

initially measured transmission of the DUT (red dots) along with the fifth-order polynomial fit in the frequency range from 0.200 THz to 0.330 THz (yellow line) used initially as a starting point $|\underline{S}_{21,\text{in}}|$ for the Monte-Carlo simulations. The confidence region associated with the confidence interval $\text{CI}_{95\%}(f)$ is shaded in green and blue below and above the polynomial line-fit, respectively. Note that 42 out of the total of 801 measured frequency points from 0.200 THz to 0.330 THz fall outside the region depicted by $\text{CI}_{95\%}(f)$, therefore counting as outliers according to our Monte-Carlo simulation. This corresponds to 5.2 % of the total data points, which is in accordance with the confidence interval definition and thereby supports the viability of the various underlying assumptions and approximations of our Monte-Carlo simulation. We further estimate the range of true DUT values associated with a 99 % confidence interval of the de-embedding-related error. To this end, we start from the DUT transmission that was obtained by the scalar de-embedding technique and subtract the expected de-embedding-related error as obtained from our Monte-Carlo simulation, see Fig. S6d. The bound associated with the 99 % confidence interval of the true DUT values is indicated by the red-shaded region in Fig. S6d. Note that, despite significant measurement inaccuracies of the feed lines and underlying assumptions of our Monte-Carlo simulation, the resulting uncertainty of the DUT transmission remains within acceptable error bounds, confirming the notion that the scalar de-embedding approach is a pragmatic approximation.

6. Characterization of THz probes (TP)

The TP were measured on a manual probing station (Cascade PM8, FormFactor GmbH), using a custom vacuum chuck attached to a manual actuator (RPP210, FormFactor GmbH) for alignment and contacting. The experimental setup, which is schematically illustrated in Fig. 4a of the main manuscript, is shown in more detail in Fig. S7, with the zoom-in providing a closer look at the samples under test. First, the probed contacting chip with the two CPW feeds $(L_\text{feed} = 1.5\,\text{mm})$ is placed on a microwave-absorbing impedance-standard substrate (ISS) holder (116-344, FormFactor GmbH) and mounted on the sample stage of the probing station. The sample chip containing the two TP is then picked up by the custom vacuum chuck and moved towards the contacting chip using the manual actuator. As mentioned in the main manuscript, the two TP protrude beyond the contour of the chip such that they are visible in the top-view camera of the probing station, having its observation direction along the positive *z*-direction in the zoom-in of Fig. S7. This arrangement allows for concurrent monitoring of the TP and of the conventional probes required for contacting of the CPW feeds on the contacting chip. For alignment of the two TP, the sample chip is first rotated about the *x*- and *y*-axis using goniometers attached to the manual actuator until it is oriented in parallel to the underlying contacting chip. Due to the comparatively large distance of $2L_\text{TP} + L_\text{conn} = 4.63\,\text{mm}$ between the opposing tips of the two TP, special care must be taken for the rotation about the *x*-axis to avoid damaging the tips during contacting. The sample chip is then moved in the (*x*,*y*)-plane for concurrent alignment of the three 100 µm-spaced tips with respect to the signal and ground conductors of the CPW feeds on both sides. Finally, the TP are carefully moved down on the CPW feeds below using the *z*-stage of the manual actuator.

For *S*-parameter measurements in the different frequency ranges from 10 MHz to 0.330 THz, we again use a VNA (N5242B PNA-X, Keysight Technologies Inc.) in conjunction with a pair of frequency-extending transmit / receive modules connected via a millimeter-wave controller (N5292A, Keysight Technologies Inc.), see Fig. S7. For all recordings, the VNA is again set to measure at 801 frequency points with an IF bandwidth of 100 Hz. For the measurement shown in Fig. 4b of the main manuscript, a total of three frequency ranges (10 MHz … 0.130 THz; 0.130 THz … 0.220 THz; 0.220 THz … 0.330 THz) are addressed by selecting corresponding extension modules and probes. For each of these frequency ranges, an LRRM calibration[11] is carried out using the manufacturer-recommended ISS (138-357, FormFactor GmbH). Our VNA system[15] relies on probes with integrated diplexers (T-Wave Dual Band Probe, T220-UBBT-GSG-100, FormFactor GmbH) to enable single-sweep measurements over the first two frequency ranges from 10 MHz to 0.220 THz. More specifically, the system combines a pair of frequency-extension modules from 10 MHz to 0.130 THz (N5295AX02, Keysight Technologies Inc.) with a second pair of frequency-extenders operating from 0.130 THz to 0.220 THz (WR5.1-VNAX, Virginia Diodes Inc., Charlottesville, USA) in the same probe. Lastly, measurements in the frequency range from 0.220 THz to 0.330 THz are carried out with a third pair of frequency-extension modules (WR3.4-VNAX, Virginia Diodes Inc.) and a corresponding set of waveguide probes (Infinity Probe i325-T-GSG-100-BT, FormFactor GmbH).

The results obtained from our measurements do not only comprise the characteristics of the two TP but also the two short CPW on the contacting chip leading from the measurement probes to the TP on each side as well as the connecting CPW on the sample chip. For de-embedding the TP, the measured *S*-parameter matrices $\underline{\mathbf{S}}_\text{meas}$ between Plane $1''$ and Plane $2''$, indicated by brown lines in Fig. 4a of the main manuscript, are converted to transfer matrices (*T*-matrices[10], see Supplementary Section 8 above, and the *T*-matrix $\underline{\mathbf{T}}_\text{meas}$ of the network can again be represented by cascading the *T*-matrices of the individual elements, leading to

$$\underline{\mathbf{T}}_\text{meas} = \underline{\mathbf{T}}_\text{feed}\,\underline{\mathbf{T}}_\text{TP}\,\underline{\mathbf{T}}_\text{conn}\,\underline{\mathbf{T}}_\text{TP}\,\underline{\mathbf{T}}_\text{feed}, \tag{5}$$

where $\underline{\mathbf{T}}_\text{feed}$, $\underline{\mathbf{T}}_\text{TP}$, and $\underline{\mathbf{T}}_\text{conn}$ represent the *T*-matrices of the CPW feed, the TP, and the connecting CPW, respectively. Note that we assume the two *T*-matrices of the two TP to be identical and labelled $\underline{\mathbf{T}}_\text{TP}$. Similarly, the

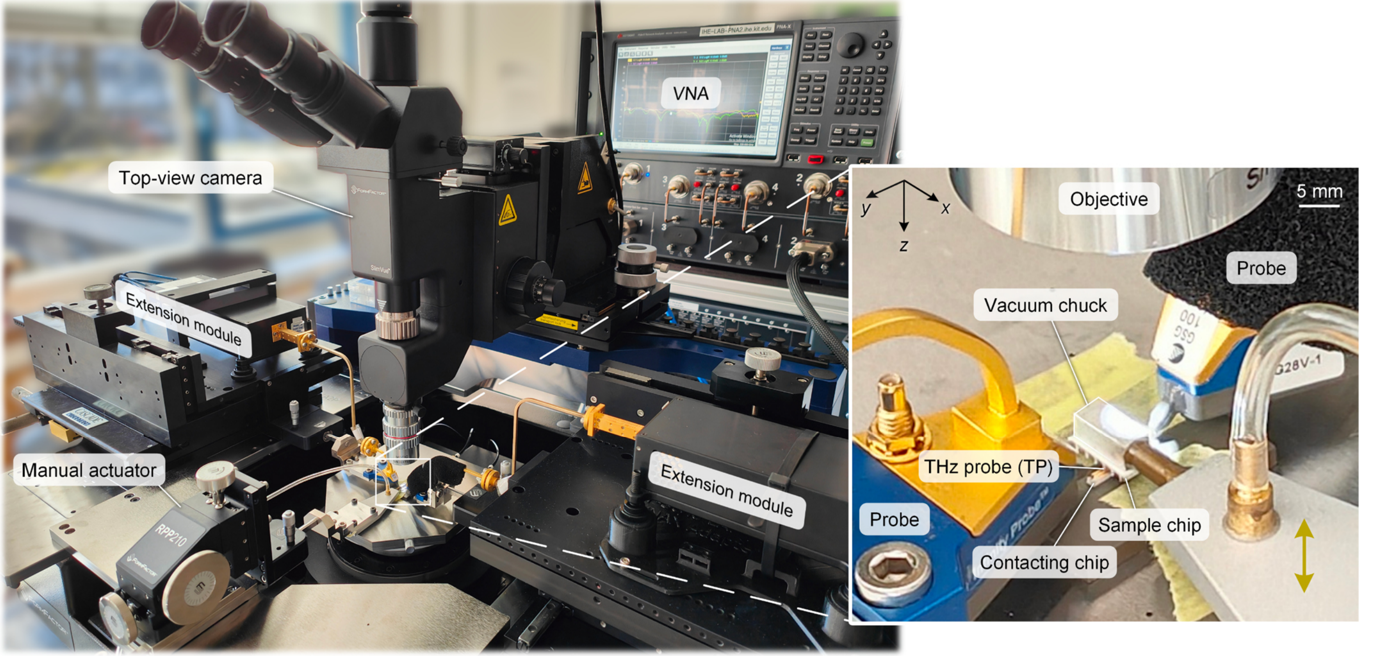

Fig. S7 | Experimental setup for characterization of THz probes (TP). The TP were measured on a manual probing station using a custom vacuum chuck attached to a manual actuator for alignment and contacting. The zoom-in provides a closer look at the sample chip, the contacting chip, and the probes used for the measurement. In a first step, the contacting chip, see Fig. 4a of the main manuscript, is placed on a microwave-absorbing ISS holder and mounted on the sample stage of the probing station, where the CPW feed lines are electrically contacted using commercially available conventional probes. The sample chip containing the TP is then picked up by the custom vacuum chuck and moved towards the contacting chip using the manual actuator. The two TP protrude beyond the contour of the chip such that they are visible in the top-view camera of the probing station. This arrangement allows for simultaneous monitoring of the TP and of the conventional probes contacting the CPW feeds on the contacting chip. After concurrent alignment of the three 100 µm-spaced tips of the TP with respect to the signal and ground conductors of the CPW feeds on each side, the TP are carefully moved down onto the contacting chip using the *z*-stage of the manual actuator. For *S*-parameter measurements in the different frequency ranges from 10 MHz to 0.330 THz, a vector network analyzer (VNA) is used in conjunction with different pairs of frequency-extending transmit / receive modules.

T-matrices of the two CPW feeds are assumed to be identical and denoted as $\underline{\mathbf{T}}_{\text{feed}}$. In a next step, we move the reference planes to Plane $1'$ and Plane $2'$ (blue lines in Fig. 4a of the main manuscript), thereby removing the influence of the two 1.5 mm-long CPW feeds. To this end, we measure the *S*-parameter matrix $\underline{\mathbf{S}}_{\text{feed,ref}}$ of an identical CPW with length L_{feed} and calculate the corresponding *T*-matrix $\underline{\mathbf{T}}_{\text{feed,ref}}$. Equation (5) can then be multiplied from both sides by the inverse matrix $\underline{\mathbf{T}}_{\text{feed,ref}}^{-1}$, which leads to

$$\underline{\mathbf{T}}_{\text{feed,ref}}^{-1}\,\underline{\mathbf{T}}_{\text{meas}}\,\underline{\mathbf{T}}_{\text{feed,ref}}^{-1} = \underline{\mathbf{T}}_{\text{feed,ref}}^{-1}\,\underline{\mathbf{T}}_{\text{feed}}\,\underline{\mathbf{T}}_{\text{TP}}\,\underline{\mathbf{T}}_{\text{conn}}\,\underline{\mathbf{T}}_{\text{TP}}\,\underline{\mathbf{T}}_{\text{feed}}\,\underline{\mathbf{T}}_{\text{feed,ref}}^{-1} = \underline{\mathbf{T}}_{\text{TP}}\,\underline{\mathbf{T}}_{\text{conn}}\,\underline{\mathbf{T}}_{\text{TP}} = \underline{\mathbf{T}}_{\text{TP-conn-TP}} \tag{6}$$

under the assumption that the measured reference CPW and the embedded CPW feeds are identical, i.e., $\underline{\mathbf{T}}_{\text{feed,ref}}^{-1}\,\underline{\mathbf{T}}_{\text{feed}} = \underline{\mathbf{T}}_{\text{feed}}\,\underline{\mathbf{T}}_{\text{feed,ref}}^{-1} = \mathbf{I}$. The extracted *T*-matrix $\underline{\mathbf{T}}_{\text{TP-conn-TP}}$ can then be converted back to the *S*-parameter matrix $\underline{\mathbf{S}}_{\text{TP-conn-TP}}$ with its complex-valued transmission and reflection coefficients $\underline{S}_{2'1'}$ and $\underline{S}_{1'1'}$, respectively. Figure S8 shows the associated transmission and reflection parameters $S_{2'1',\text{dB}} = 10\log_{10}(|\underline{S}_{2'1'}|^2)$ (blue curve) and $S_{1'1',\text{dB}} = 10\log_{10}(|\underline{S}_{1'1'}|^2)$ (green curve), which are in good agreement with the associated simulation (dashed black lines).

While the previously extracted parameters $S_{2'1',\text{dB}}$ and $S_{1'1',\text{dB}}$ already give an indication about the performance of the pair of TP, the 3.8 mm-long connecting CPW contained in $\underline{\mathbf{S}}_{\text{TP-conn-TP}}$ still contributes significantly to the overall loss. We therefore estimate the insertion loss of a single TP (Fig. 4b of the main manuscript) by using a scalar correction to compensate for the losses caused by all concatenated CPW ($L_{\text{feed}} + L_{\text{conn}} + L_{\text{feed}} = 6.8\,\text{mm}$) in the arrangement between Plane $1''$ and Plane $2''$. To this end, we start from the measured transmission of the full arrangement $S_{2''1'',\text{meas,dB}} = 10\log_{10}(|\underline{S}_{2''1'',\text{meas}}|^2)$ and we use a 6.8 mm-long reference CPW on the contacting chip to obtain the compound transmission of the 3.8 mm-long connecting line and the two 1.5 mm-long feed lines, which we denote as $S_{2''1'',\text{ref,dB}} = 10\log_{10}(|\underline{S}_{2''1'',\text{ref}}|^2)$. The transmission of each of the two TP is then estimated by taking the difference of the two dB-values and dividing the result by two,

$$S_{21,\text{dB}} = \left(S_{2''1'',\text{meas,dB}} - S_{2''1'',\text{ref,dB}}\right)/2. \tag{7}$$

The resulting values are plotted in Fig. 4b of the main manuscript.

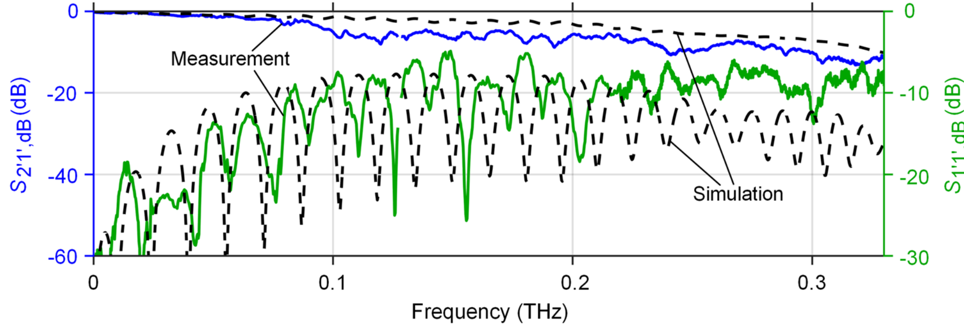

Fig. S8 | De-embedded measurements between reference Plane $1'$ and Plane $2'$ comprising the pair of TP and the connecting CPW. The raw measurements are taken between Plane $1''$ and Plane $2''$ with the setup depicted in Fig. S7, see brown lines in Fig. 4a of the main manuscript. These measurements do not only comprise the characteristics of the two TP but also the two short CPW on the contacting chip, leading from the measurement probes to the TP on each side, as well as the connecting CPW on the sample chip. Using Eq. (6), the reference planes can be moved to Plane $1'$ and Plane $2'$ (blue lines in Fig. 4a of the main manuscript), thereby removing the influence of the two 1.5 mm-long CPW feeds. The associated transmission and reflection parameters $S_{2'1',\mathrm{dB}} = 10\log_{10}(|\underline{S}_{2'1'}|^2)$ (blue curve) and $S_{1'1',\mathrm{dB}} = 10\log_{10}(|\underline{S}_{1'1'}|^2)$ (green curve) are in good agreement with the associated simulation (dashed black lines). Note that the loss of the 3.8 mm-long connecting CPW still contributes significantly to the overall loss. This contribution is removed by using a scalar correction technique, leading to the transmission characteristics of a single TP.

For evaluating the contacting repeatability of the TP, we performed measurements in the frequency range from 0.220 THz to 0.330 THz for a total of $N = 50$ contacting cycles, see Fig. 4c of the main manuscript. To this end, we used the *z*-stage of the manual actuator to repeatedly lift the sample chip up and lower it back down without intermediate re-alignment. For all measurements, we calculated the estimated transmission through a single TP using Eq. (7) and extracted the corresponding linear magnitudes $|\underline{S}_{21}|_N = 10^{S_{21,\mathrm{dB}_N}/20}$. With the average transmission magnitude $\overline{|\underline{S}_{21}|} = \left(\sum_N |\underline{S}_{21}|_N\right)/N$, we can then express the measurement deviation $\Delta|\underline{S}_{21}|_N$ for the N-th measurement as the difference to the mean transmission,

$$\Delta|\underline{S}_{21}|_N = |\underline{S}_{21}|_N - \overline{|\underline{S}_{21}|}. \tag{8}$$

For the $N = 50$ contacting cycles, a maximum magnitude deviation of $\Delta|\underline{S}_{21}|_{\max} \approx 5\times10^{-3}$ was measured, corresponding to a maximum relative error of 0.6 %. Figure 4c of the main manuscript shows the associated standard deviation of the amplitude-transmission magnitude

$$\sigma\left(|\underline{S}_{21}|\right) = \sigma\left(\Delta|\underline{S}_{21}|\right) = \sqrt{\frac{1}{N-1}\sum_N\left(\Delta|\underline{S}_{21}|_N\right)^2} \tag{9}$$

over the measured frequency range. We found a remarkably low maximum standard deviation of $\sigma(|\underline{S}_{21}|)_{\max} \approx 2\times10^{-3}$ (corresponding to –55 dB) near 0.32 THz.

7. Characterization of THz antennas (TA)

The TA were measured on a probe-based free-space antenna measurement setup[16,17], which allows to move a receive antenna around a contacted antenna-under-test (AUT) and to record the radiation pattern. The receive antenna and the AUT are oriented such that both antennas are co-polarized. A picture of the experimental setup is shown in Fig. S9, and further explanations of the setup and the calibration steps summarized in the following can be found in the associated publications[16,17]. For measurement in the frequency range from 0.220 THz to 0.325 THz, we again used our VNA (N5242A PNA-X, Keysight Technologies Inc.) in conjunction with a frequency-extension module (V03VNA2-T/R-A, OML Inc.) connected via a millimeter-wave controller (N5261A, Keysight Technologies Inc.). The VNA is again set to measure at 801 frequency points with an IF bandwidth of 100 Hz.

The calibration of the setup was carried out in multiple steps: First, a scalar gain calibration is performed using a standard horn antenna (QWH-3PRR00, QuinStar Technology Inc., Torrance, USA) with known gain G_{horn} connected to the extension module as the transmitter. From the measured transmission $\underline{S}_{21,\mathrm{horn}}$, the system characteristics including the free-space loss and the gain of the receive antenna can thereby be determined as

$$G_{\mathrm{sys}} = |\underline{S}_{21,\mathrm{horn}}|^2 / G_{\mathrm{horn}}\,. \tag{10}$$

Next, the known transmitter antenna is removed, and a waveguide probe (Infinity Probes i325-T-GSG-100-BT, FormFactor GmbH) is instead connected to the extension module. To remove the influence of the probe, an additional one-port short-open-load (SOL) calibration[17,18] is carried out using an ISS (138-357, FormFactor GmbH).

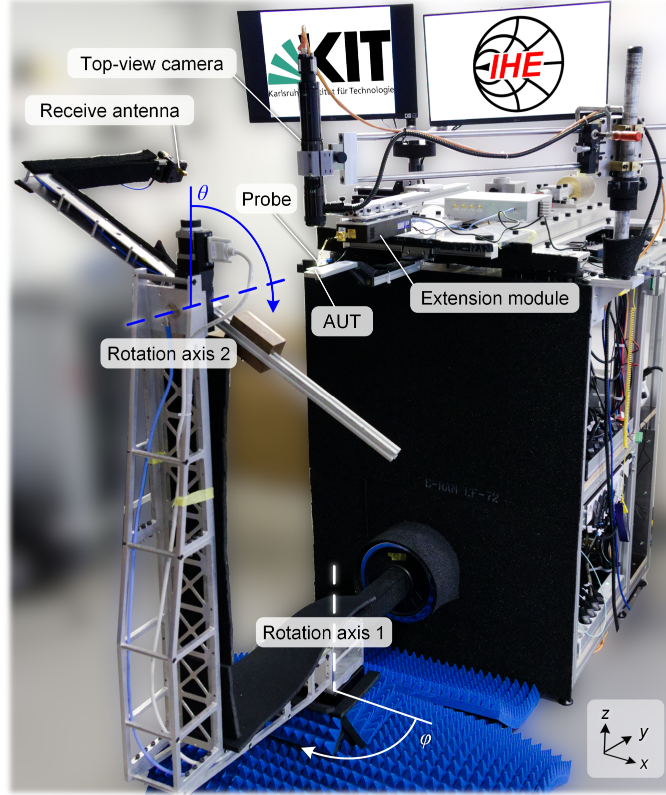

Fig. S9 | Experimental setup for characterization of THz antennas (TA). The devices on a probe-based free-space antenna characterization setup[16,17], which allows to move a receive antenna around a contacted antenna-under-test (AUT) while recording the direction-dependent radiation pattern of the latter. For measurements in the frequency range from 0.220 THz to 0.325 THz, a vector network analyzer is used in conjunction with a frequency-extension module. A top-view camera helps in contacting the AUT and is swiveled to the side once the sample is contacted to not influence the measurement of the radiation pattern. The radiation pattern can be recorded by moving the receive antenna around the AUT at a constant distance of roughly 38 cm using a two-axis rotational system. For the antenna pattern shown in Fig. 5b of the main manuscript, the motor controlling the first rotation axis was set to a fixed position corresponding to an azimuth of $\varphi = 0°$, while the stepping motor of the second stage was used to move the receive antenna around the AUT by sweeping the elevation angle θ . This corresponds to a measurement in the so-called *H*-plane of the antenna – the corresponding trajectory is illustrated by a blue half-circle in Fig. 5a of the main manuscript. For each elevation angle θ, we extract the realized gain $G_{\mathrm{R,TA}}(\varphi = 0°, \theta)$ from the corresponding *S*-parameter measurement $\underline{S}_{21,\mathrm{TA}}(\varphi = 0°, \theta)$ after performing a dedicated gain and SOL calibration.

This calibration allows to determine the three elements of a one-port SOL error-adapter matrix, $\underline{\mathbf{E}} = \begin{pmatrix} \underline{e}_{00} & \underline{e}_{01} \\ \underline{e}_{10} & \underline{e}_{11} \end{pmatrix}$, where the elements $\underline{e}_{00}$, $\underline{e}_{11}$, and $\underline{e}_{10}\underline{e}_{01}$ are related to the directivity, the source matching, and the reflection tracking, respectively. Assuming a reciprocal error network ($\underline{e}_{10} = \underline{e}_{01}$), the transmission of the probe is given by $G_{\mathrm{probe}} = |\underline{e}_{10}\underline{e}_{01}|$.

In a next step, the AUT is contacted contacted, and the direction-dependent realized gain calculated from the measured direction-dependent transmission $\underline{S}_{21,\mathrm{TA}}(\varphi, \theta)$ and the known probe transmission G_{probe},

$$G_{\mathrm{R,TA}}(\varphi, \theta) = |\underline{S}_{21,\mathrm{TA}}(\varphi, \theta)|^2 \big/ (G_{\mathrm{sys}} G_{\mathrm{probe}}). \tag{11}$$

In these relations, the direction is defined by the azimuth angle φ and the elevation angle θ as illustrated in Fig. S9. The measured TA was manufactured directly at the end of a transmission line in the center of a chip, thereby allowing easy handling and contacting of the CPW feed during measurement. A top-view camera helps contacting the AUT and is swiveled to the side once the sample is contacted to not influence the measurement of the radiation pattern. The direction-dependent radiation pattern can be measured by moving the receive antenna around the AUT at a constant distance of roughly 38 cm using a two-axis rotational system. For the antenna pattern shown in Fig. 5b of the main manuscript, the motor controlling the first rotation axis (Rotation axis 1 in Fig. S9) was set to a fixed position, corresponding to an azimuth of $\varphi = 0°$, while the stepping motor of the second stage was used to move the receive antenna around the AUT by sweeping the elevation angle θ from $\theta_{\mathrm{min}} = -90°$ to $\theta_{\mathrm{max}} = +90°$ (Rotation axis 2 in Fig. S9) in steps of 2° for a total of 91 measurements. The trajectory of the receive antenna is indicated by a blue half-circle in Fig. 5a of the main manuscript. For each elevation angle θ, we extracted the realized gain $G_{\mathrm{R,TA}}(\varphi = 0°, \theta)$ from the corresponding calibrated *S*-parameter measurement $\underline{S}_{21,\mathrm{TA}}(\varphi = 0°, \theta)$ using Eq. (11). The gain can finally be expressed in decibels as $G_{\mathrm{R,TA,dBi}}(\varphi = 0°, \theta) = 10 \log_{10} G_{\mathrm{R,TA}}(\varphi = 0°, \theta)$. The radiation pattern (*H*-plane) was recorded for a frequency of 0.274 THz, where a maximum realized gain of 5.5 dBi was measured in the direction perpendicular to the substrate, i.e., for an elevation angle of $\theta = 0°$.

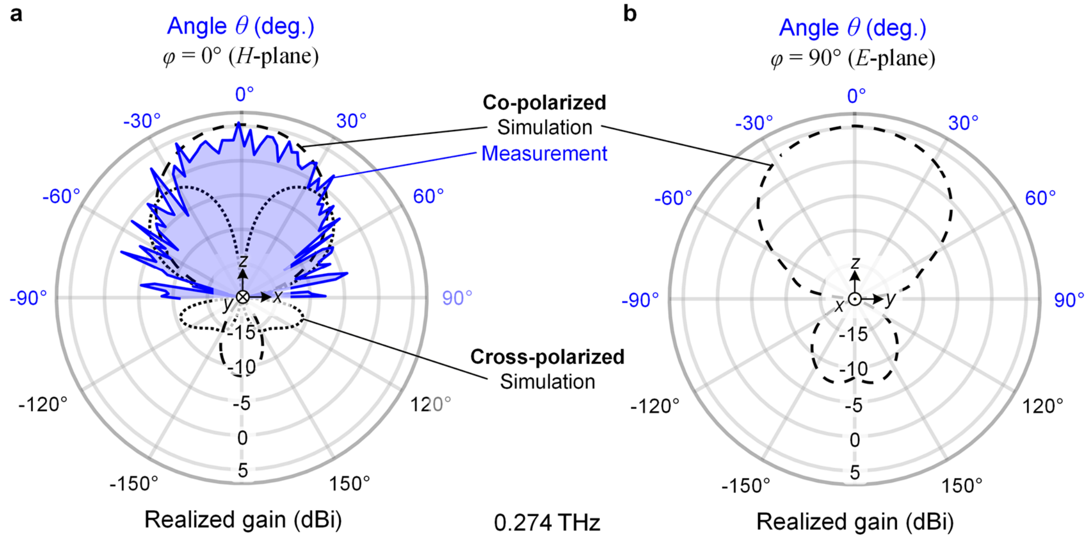

Fig. S10 | Simulated radiation pattern of our THz antenna (TA) for different elevation angles θ at 0.274 GHz. a Radiation pattern in the *H*-plane, i.e., for a θ-sweep at φ = 0°, see Fig. S9 for the definition of the coordinate system. The corresponding trajectory for the movement of the receive antenna is illustrated by a blue half-circle in Fig. 5a of the main manuscript. The simulated co-polarization and cross-polarization component of the realized gain $G_{\mathrm{R,TA}}(\varphi = 0°, \theta)$ are depicted by the dashed and dotted black lines, respectively. The experimentally measured co-polarization component of the realized gain in the upper half-space is given by the blue trace and coincides reasonably well with the simulation, hence confirming the viability of the simulation model. **b** Radiation pattern in the *E*-plane of the antenna (θ-sweep at φ = 90°). The dashed black line represents the simulated co-polarization component of the realized gain $G_{\mathrm{R,TA}}(\varphi = 90°, \theta)$. The cross-polarization component vanishes for this specific plane due to symmetry of the antenna.

Note that our experiments were limited to measuring the co-polarized component of the radiation pattern in the *H*-plane only. The reason was that probe-fed antenna measurement setups at sub-THz frequencies such as the one used in our work typically suffer from reflections and scattering from the probe body, self-radiation of the probe tip, as well as parasitic coupling between the probe and the antenna[19,20]. These effects lead to significant impairments of measurements in planes that are normal to the substrate and oriented along the feed direction of the probe[21]. In the setup shown in Fig. S9, this plane, which corresponds to φ = 90°, coincides with the *E*-plane of the THz antenna and was discarded from the measurements. Similarly, the rather weak cross-polarized component in the *H*-plane was not acquired since the radiation levels are approaching values that cannot be reliably discriminated from spurious radiation that originates directly from the measurement probe, despite careful alignment and calibration. To still provide a complete picture of the antenna's far-field behavior, we have simulated the overall radiation pattern of the antenna to include the co- and cross-polarization components of the realized gain for both the *H*-plane (θ-sweep at φ = 0°) and the *E*-plane (θ-sweep at φ = 90°), see Fig. S10. In Fig. S10a, the dashed black line represents the co-polarization component of the realized gain $G_{\mathrm{R,TA,co}}(\varphi = 0°, \theta)$ in the *H*-plane, whereas the cross-polarization component $G_{\mathrm{R,TA,cross}}(\varphi = 0°, \theta)$ is represented by the dotted black line. We have also included the experimentally measured co-polarization component of the realized gain in the upper half-space region as depicted in Fig. 5b in the main manuscript, see blue line. Similarly, the dashed black line in Fig. S10b represents the co-polarization component $G_{\mathrm{R,TA,co}}(\varphi = 90°, \theta)$ in the *E*-plane. Note that the cross-polarization component $G_{\mathrm{R,TA,cross}}(\varphi = 90°, \theta)$ in the *E*-plane is not shown, as it vanishes for this specific plane due to the symmetry of the antenna structure. For the *H*-plane, Fig. S10a, the simulated realized antenna gain for the co-polarized component coincides reasonably well with its measured counterpart, confirming the viability of the simulation model. The levels of cross-polarization distinction (XPD) obtained from the simulation are typical for on-chip antennas with limited ground planes operating in this frequency range[22,23]. Higher XPD values for slot antennas are typically only achieved by highly symmetric structures such as cross-dipole array arrangements with symmetric or differential feeding[24,25].

8. Conversion between *S*-parameters and *T*-matrix parameters

For conversion between *S*-matrix parameters and *T*-matrix parameters, we use the following relations[10,26]:

$$\underline{\mathbf{T}} = \begin{pmatrix} \underline{T}_{11} & \underline{T}_{12} \\ \underline{T}_{21} & \underline{T}_{22} \end{pmatrix} = \begin{pmatrix} 1/\underline{S}_{21} & -\underline{S}_{22}/\underline{S}_{21} \\ \underline{S}_{11}/\underline{S}_{21} & -\det(\underline{\mathbf{S}})/\underline{S}_{21} \end{pmatrix}, \tag{12}$$

$$\underline{\mathbf{S}} = \begin{pmatrix} \underline{S}_{11} & \underline{S}_{12} \\ \underline{S}_{21} & \underline{S}_{22} \end{pmatrix} = \begin{pmatrix} \underline{T}_{21}/\underline{T}_{11} & \det(\underline{\mathbf{T}})/\underline{T}_{11} \\ 1/\underline{T}_{11} & -\underline{T}_{12}/\underline{T}_{11} \end{pmatrix}. \tag{13}$$

In these two relations, $\det(\underline{\mathbf{S}}) = \underline{S}_{11}\underline{S}_{22} - \underline{S}_{12}\underline{S}_{21}$ and $\det(\underline{\mathbf{T}}) = \underline{T}_{11}\underline{T}_{22} - \underline{T}_{12}\underline{T}_{21}$ refer to the determinant of the *S*-parameter matrix $\underline{\mathbf{S}}$ and *T*-parameter matrix $\underline{\mathbf{T}}$, respectively.

References

1. Wylde, R. J. Millimetre-wave Gaussian beam-mode optics and corrugated feed horns. *IEE Proceedings H Microwaves, Optics and Antennas* **131**, 258–262 (1984).
2. Bartley, P. G. & Begley, S. B. Improved free-space *S*-parameter calibration. in *IEEE Instrumentation and Measurement Technology Conference Proceedings* 372–375 (IEEE, 2005). doi:10.1109/IMTC.2005.1604138.
3. Swissto12 SA. webMCK - User guide, Rev: 1.3. 1–13 (2021).
4. Wang, Y., Shang, X., Ridler, N. M., Huang, T. & Wu, W. Characterization of dielectric materials at WR-15 band (50–75 GHz) using VNA-based technique. *IEEE Trans Instrum Meas* **69**, 4930–4939 (2020).
5. Baker-Jarvis, J., Vanzura, E. J. & Kissick, W. A. Improved technique for determining complex permittivity with the transmission / reflection method. *IEEE Trans Microw Theory Tech* **38**, 1096–1103 (1990).
6. Baker-Jarvis, J., Janezic, M. D., Grosvenor, J. H. Jr. & Geyer, R. G. Transmission/reflection and short-circuit line methods for measuring permittivity and permeability. *NIST Technical Note 1355.* https://nvlpubs.nist.gov/nistpubs/Legacy/TN/nbstechnicalnote1355r.pdf (1992).
7. Sahin, S., Nahar, N. K. & Sertel, K. Dielectric properties of low-loss polymers for mmW and THz applications. *J Infrared Millim Terahertz Waves* **40**, 557–573 (2019).
8. Kazemipour, A. *et al.* Analytical uncertainty evaluation of material parameter measurements at THz frequencies. *J Infrared Millim Terahertz Waves* **41**, 1199–1217 (2020).
9. Samuel Lesko. Advantages of measuring surface roughness with white light interferometry. *Application Note 575.* https://www.photonics.com/White_Papers/Advantages_of_Measuring_Surface_Roughness_with/wpp1886 (2020).
10. Pozar, D. M. *Microwave Engineering, 4th ed.* (Wiley, 2012).
11. Davidson, A., Jones, K. & Strid, E. LRM and LRRM calibrations with automatic determination of load inductance. in *ARFTG Conference Digest* 57–63 (IEEE, 1990). doi:10.1109/ARFTG.1990.323996.
12. Keysight Technologies Inc. De-embedding and embedding *S*-parameter networks using a vector network analyzer. *Application Note 5980-2784EN.* https://www.keysight.com/de/de/assets/7018-06806/application-notes/5980-2784.pdf (2017).
13. Ye, X. De-embedding errors due to inaccurate test fixture characterization. *IEEE Electromagn Compat Mag* **1**, 75–78 (2012).
14. Jones, R. D. *et al.* Microstrip and grounded CPW calibration kit comparison for on-wafer transistor characterization from 220 GHz to 325 GHz. in *IEEE BiCMOS and Compound Semiconductor Integrated Circuits and Technology Symposium (BCICTS)* 124–127 (IEEE, 2023) doi:10.1109/bcicts54660.2023.10310853.
15. Keysight Technologies Inc. 170 GHz / 220 GHz broadband vector network analysis solution for on-wafer millimeter-wave component characterization. *Technical Overview 3121-1515EN.* https://www.keysight.com/de/de/assets/3121-1515/technical-overviews/170GHz-220GHz-Broadband-Vector-Network-Analysis-Solution.pdf (2022).
16. Zwick, T., Baks, C., Pfeiffer, U. R., Liu, D. & Gaucher, B. P. Probe based MMW antenna measurement setup. in *IEEE Antennas and Propagation Society Symposium* 747–750 (IEEE, 2004). doi:10.1109/APS.2004.1329778.
17. Beer, S. & Zwick, T. Probe based radiation pattern measurements for highly integrated millimeter-wave antennas. in *Proceedings of the Fourth European Conference on Antennas and Propagation* 1–5 (2010).
18. Bianco, B., Corana, A., Ridella, S. & Simicich, C. Evaluation of errors in calibration procedures for measurements of reflection coefficient. *IEEE Trans Instrum Meas* **27**, 354–358 (1978).
19. Reniers, A. C. F., van Dommele, A. R., Smolders, A. B. & Herben, M. H. A. J. The influence of the probe connection on mm-wave antenna measurements. *IEEE Trans. Antennas Propagat.* **63**, 3819–3825 (2015).
20. Hebeler, J., Zwick, T. & Bhutani, A. Radiation behaviour of mm-wave on-wafer probes in H-band and the influence on antenna measurements. *Electronics Letters* **60**, (2024).
21. Hebeler, J. *et al.* On-chip CMOS shorted bow-tie antenna enhanced by 3D printed parasitic resonator operating around 246 GHz. *IEEE Access* **13**, 65955–65965 (2025).
22. Oh, S. & Oh, J. 140-GHz Affordable miniaturized array antenna-on-package for sub-THz transceiver. *IEEE Access* **11**, 132780–132791 (2023).
23. Aqlan, B., Himdi, M., Vettikalladi, H. & Le-Coq, L. Experimental realization of sub-THz circularly polarized antenna based on metasurface superstrate at 300 GHz. *Materials* **14**, 4796 (2021).
24. Tan, X., Mei, X. & Wu, K.-L. XPD enhancement of dipole antenna arrays by inducing coherent current from feeding line. *IEEE Trans. Antennas Propagat.* **71**, 3950–3958 (2023).
25. Zhou, H., Lu, Y., You, Q., Wang, Y. & Huang, J. Wideband and high cross-polarization discrimination 45° linearly polarized slot array antenna without cavity-backed layer. *Antennas Wirel. Propag. Lett.* **21**, 2005–2009 (2022).
26. Frickey, D. A. Conversions between *S*, *Z*, *Y*, *H*, *ABCD*, and *T* parameters which are valid for complex source and load impedances. *IEEE Trans Microw Theory Tech* **42**, 205–211 (1994).